Supporting information

Electrospun Ru-RuO$_2$/MoO$_3$ Carbon Nanorods with Multi-active Components: A Pt-like Catalyst for Hydrogen Evolution Reaction

Libing Fan,[a,b] Qun Li[b,c], Dewen Wang,[b,c] Tian Meng,[b,c] Mengxia Yan,[b,c] Zhicai Xing[b], Erkang Wang,[a,b,c] and Xiurong Yang[*b,c]

[a]College of Chemistry, Jilin University, Changchun 130012, China

[b]State Key Laboratory of Electroanalytical Chemistry, Changchun Institute of Applied Chemistry, Chinese Academy of Sciences, Changchun 130022, Jilin, China

[c]School of Applied Chemistry and Engineering, University of Science and Technology of China, Hefei 230026, China

[*]E-mail: xryang@ciac.ac.cn, Tel: +86-0431-85262056.

Materials and chemicals

The following reagents were analytical-grade and utilized directly without further purification: ruthenium (III) chloride anhydrous ($RuCl_3$, Ru content 45-55 %, Aldrich), ammonium molybdate tetrahydrate ((NH_4)$_3Mo_7O_{24}\cdot4H_2O$, 99 %, Beijing Chemical works), polyvinylpyrrolidone (PVP, Mw ≈ 1300000, Aladdin), *N, N*-dimethylformamide (DMF, Sinopharm Chemical Reagent Co. Ltd), potassium hydroxide (KOH, 85 %, Beijing Chemical works), carbon paper (CP, Toray Industries Co., Ltd.), Pt/C (20 wt %, Aldrich), Nafion (5 wt %, Aldrich). Deionized water (18.25 MΩ. cm) was used in our experiment.

Preparation of Ru-RuO$_2$/MoO$_3$ CNRs-T

17.66 mg of (NH_4)$_3Mo_7O_{24}\cdot4H_2O$ (0.1 mmol of Mo) and 41.48 mg of $RuCl_3$ (0.2 mmol of Ru) were dispersed in 7 mL of DMF with magnetic agitation at room temperature for 2 h. 1 g of PVP was added into above mixture and stirred overnight to form a homogeneous viscous spinning solution. Electrospinning was implemented to fabricate the composite nanofibers which is contained Ru and Mo elements. Detailedly, the resulting solution was transferred into 10 mL plastic syringe equipped with a 20# stainless steel needle connected to positive high voltage power supply of 16 kV, the flow rate of spinning solution was 5 μL·min^{-1}, and a piece of grounded aluminum foil as a collector and 20 cm from the needle tip. After the power supply was applied, the spinning solution was ejected from the needle tip under the action of electrostatic field. The nanofibers was collected on aluminum foil after being stretched and solidified in air, hereinafter marked as Ru-Mo/PVP composite nanofibers. Afterwards, the Ru-Mo/PVP composite nanofibers were first stabilized and pre-oxidized at 200 °C for 2 h with a heating rate of 2 °C min^{-1}, and then calcinated at different temperatures for 3 h with a heating rate of 5 °C min^{-1} under atmospheric conditions. After the calcination, a series of electrocatalysts were obtained in the form of black powders and was expressed as Ru-RuO$_2$/MoO$_3$ CNRs-T, where T represents the calcination temperature of 250, 300, 350, and 400 °C, respectively.

Preparation of Ru-RuO$_2$ CNPs

The synthetic procedures of Ru-RuO$_2$ CNPs were similar to that of the Ru-RuO$_2$/MoO$_3$ CNRs-350 in the absence of (NH_4)$_3Mo_7O_{24}\cdot4H_2O$.

Preparation of MoO$_3$ CNRs

The synthetic procedures of MoO_3 CNRs were similar to that of the Ru-RuO_2/MoO_3 CNRs-350 in the absence of $RuCl_3$.

Electrochemical measurements

4 mg of as-prepared electrocatalysts were dispersed in a mixture of 1 mL of DMF and 20 μL of Nafion solution (5 wt%), and was ultrasonicated for at least 1 h to form the uniform catalyst ink. 5 μL of the well-dispersed catalysts ink was transferred onto a piece of pre-treated carbon paper (CP) electrode (area of 0.5 ×0.6 cm^2) for four times (20 μL in total) and dried at 60 °C, with the loading amount of 0.261 mg·cm^{-2}. Electrochemical tests of all catalysts were performed by using CHI 660E electrochemical workstation (CH Instruments, Inc., Shanghai) with the typical three-electrode configuration in 1.0 M KOH. The catalyst-loaded CP, saturated calomel electrode (SCE, Hg/Hg_2Cl_2 saturated with KCl solution) and graphite rod were invoked as the working electrode, reference electrode and counter electrode, respectively. Unless otherwise noted, the potentials reported in our manuscript were manually iR-corrected and calibrated to reversible hydrogen electrode (RHE) by adding the value of (0.242 + 0.059 pH) V.

Prior to linear sweep voltammetry (LSV) tests, the electrocatalysts were activated and stabilized through 20 cycles of cyclic voltammetry (CV). Polarization curves for HER acquired from LSV were recorded on the catalyst-loaded CP at a scan rate of 5 mV·s^{-1} from 0.1 V to -0.5 V vs. RHE. Double layer capacitance (C_{dl}) was determined by recording CV at different scan rates (10 - 200 mV·s^{-1}) in the range of 0.1 - 0.2 V vs. RHE to assess the electrochemical surface areas (ECSA) of the catalysts. Electrochemical impedance spectra (EIS) measurement was performed at overpotential of 100 mV along with the frequency range from 10^5 Hz to 10^{-1} Hz. Both CV (potential window: 0.1 V to -0.5 V vs. RHE, scan rate: 100 mV·s^{-1}) and chronoamperometry (overpotential: 10 mV) were used for stability tests.

Characterizations

The thermal preperty of Ru-Mo/PVP composite nanofibers was measured by thermogravimetric analyzer and differential scanning calorimeter (TGA/DSC, TA Instruments TGA500, USA). The phase compositions of electrocatalysts were analysized by X-ray diffraction (XRD) on a D8 ADVANCE diffractometer (Bruker, Germany) in the 2θ range from 10 to 90°. The scanning electron microscopy (SEM, OXFORD Instrument XMAX and Zeiss) equipped with energy-dispersive X-ray spectrometer (EDS), transmission electron microscopy (Hitachi and Tecnai G2 F20 S-

TWIN) were carried out to characterize the surface morphologies, nano-structure and elemental composition of the catalysts. The elements electronic state on the surface of catalysts were scrutinized by X-ray photoelectron spectroscopy (XPS, ThermoFischer, ESCALAB 250Xi). The ratio of Ru and Mo in catalysts were measured by inductively coupled plasma optical emission spectrometry (ICP-OES, Thermo ICAP 6300). The Brunauer-Emmett-Teller (BET) surface area and the distribution of pore size were calculated from N_2 adsorption-desorption isotherms measured at 77 K on an Autosorb iQ Station.
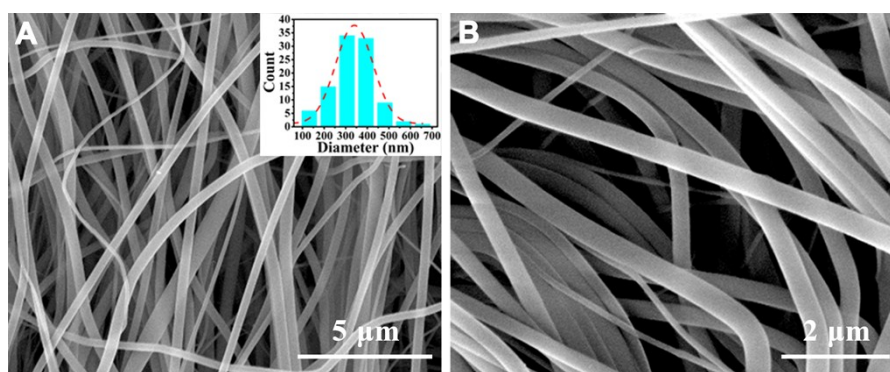
Fig. S1 (A) Low- and (B) high-magnification SEM images of Ru-Mo/PVP composite nanofibers (inset: histograms of the diameter distribution).
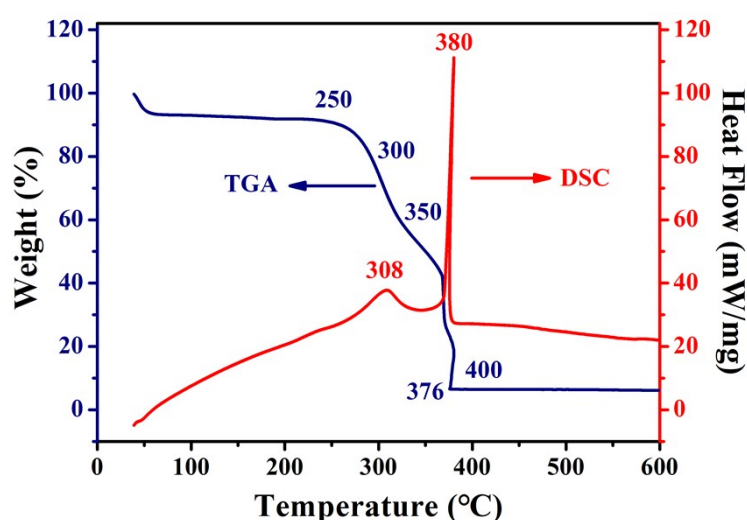
Fig. S2 TGA and DSC curves of the Ru-Mo/PVP composite nanofibers.

TGA and DSC curves of Ru-Mo/PVP composite nanofibers were obtained under air atmosphere with a heating rate of 5 °C min^{-1}, as shown in **Fig. S2**. The weight loss before 200 °C mainly comes from the volatilization of residual solvent and surface adsorbed water in Ru-Mo/PVP composite nanofibers. When the temperature rises to 250 °C, the PVP polymer begins to decompose and $(NH_4)_3Mo_7O_{24}$ is decomposed into NH_3, H_2O and MoO_3, as well as the $RuCl_3$ is transformed into RuO_2 and/or Ru. Between 250 °C and 376 °C, rapid combustion and decomposition of PVP polymer occurs, leading to the sharp weight loss in TGA curve and narrow endothermic peak at 380 °C in DSC curve. With further increase in temperature, no obvious weight loss from the TGA curve and no thermal peak from the DSC curve are found. Therefore, the temperature of 250, 300, 350, and 400 °C were selected in the subsequent experiments to investigate the effect of calcination temperature on the catalytic activity of the electrospun-catalysts.
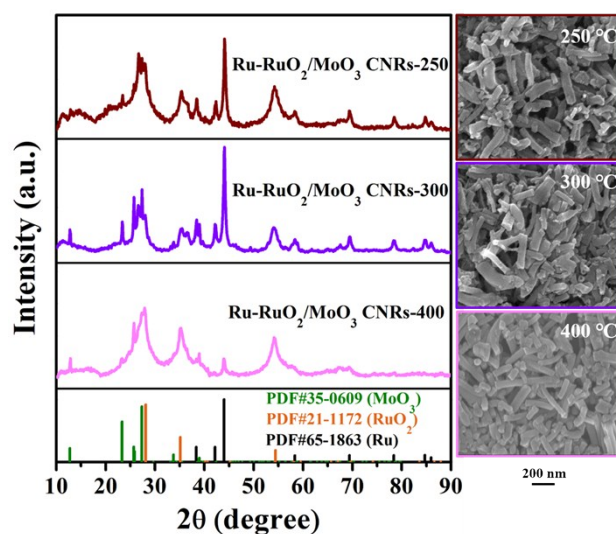
Fig. S3 XRD patterns and the corresponding SEM images of Ru-RuO$_2$/MoO$_3$ CNRs-T (T= 250, 300, and 400 °C).

The diffraction peaks of metallic Ru are narrow and strong when the annealing temperature at 250 and 300 °C. As the temperatures rise to 350 and 400 °C, the characteristic peaks of metallic Ru become weaker and some small diffraction peaks almost disappear, on the contrary, the corresponding diffraction peaks of RuO$_2$ enhanced. It could imply that higher calcination temperature tends to generate RuO$_2$ rather than metallic Ru. In other words, the calcination temperatures change the ratio of Ru/RuO$_2$ in the catalyst. The peaks of Ru-RuO$_2$/MoO$_3$ CNRs-T located at 2θ = 38.2, 42.2, 44.0, 58.2, 69.3, 78.4 and 84.7° respectively correspond to the (100), (002), (101), (102), (110), (103) and (112) planes of hexagonal phase Ru, and the peaks at 27.8, 35.0 and 54.3° are indexed to the (110), (101) and (211) planes of RuO$_2$ phase[1,2]. The diffraction peaks of MoO$_3$ at 12.7 (020), 23.2 (110), 25.6 (040), 27.8 (021), and 49.6° (002) were also observed in XRD patterns of the Ru-RuO$_2$/MoO$_3$ CNRs-350[3].
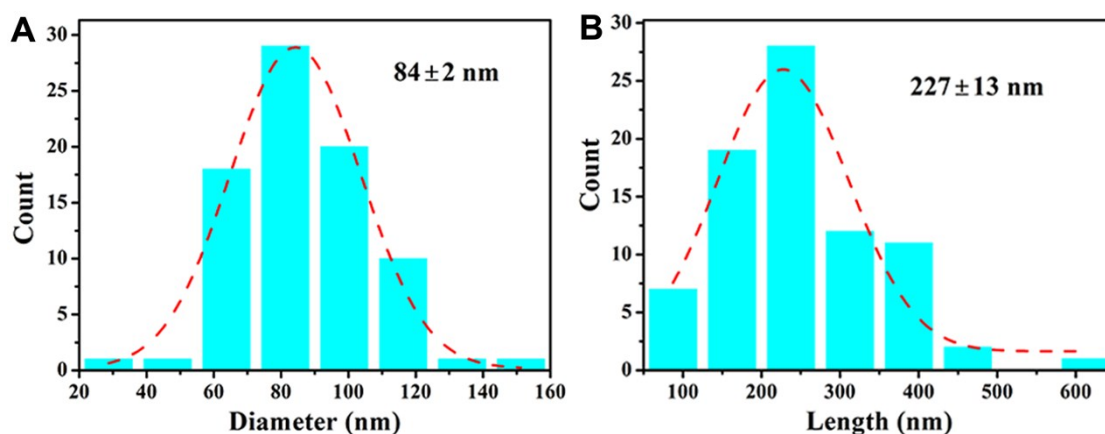
Fig. S4 Histograms of the (A) diameter and (B) length distribution for the Ru-RuO$_2$/MoO$_3$ CNRs-350.
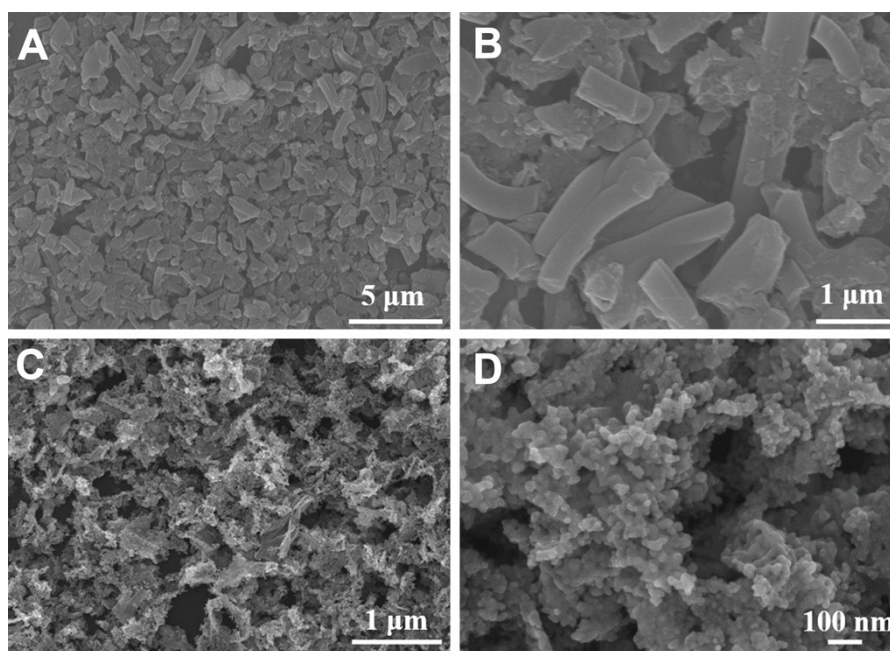
Fig. S5 (A, C) Low- and (B, D) high-magnification SEM images of (A, B) MoO$_3$ CNRs and (C, D) Ru-RuO$_2$ CNPs.

For MoO$_3$ CNRs and Ru-RuO$_2$ CNPs, the content of metal precursor in their corresponding as-spun polymer nanofibers is relatively low, resulting in the fact that the aggregation speed of metal-oxides and/or metal are lower than the decomposition rate of the PVP template during the calcination process. Therefore, the perfect nanorod-structure is not form in these two catalysts.
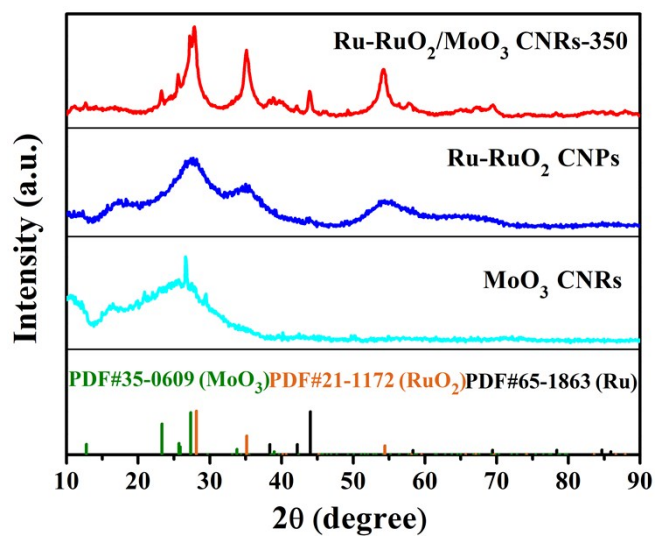
Fig. S6 XRD patterns of Ru-RuO$_2$/MoO$_3$ CNRs-350, Ru-RuO$_2$ CNPs, and MoO$_3$ CNRs.
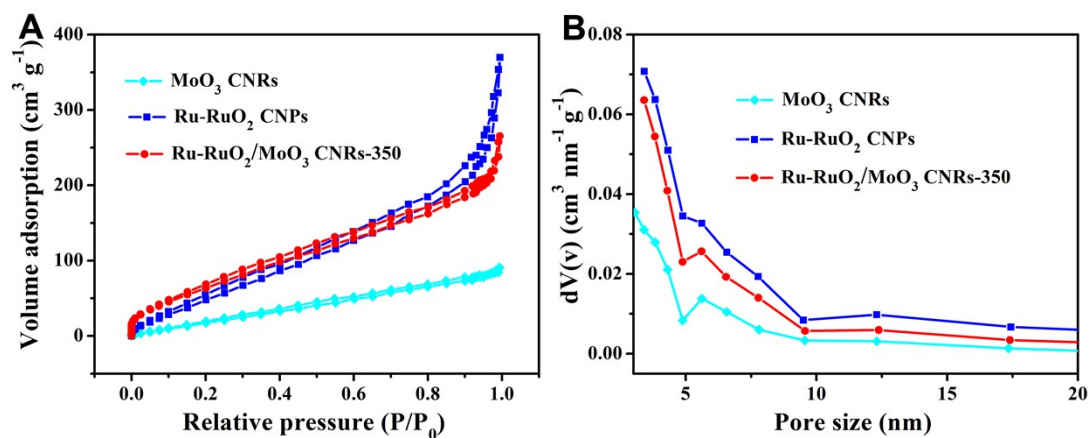
Fig. S7 (A) N$_2$ adsorption-desorption isotherms and (B) the corresponding BJH pore size distribution curves of MoO$_3$ CNRs, Ru-RuO$_2$ CNPs, and Ru-RuO$_2$/MoO$_3$ CNRs-350. The surface areas are 116.5, 269.3, and 260.4 m^2 g^{-1} for MoO$_3$ CNRs, Ru-RuO$_2$ CNPs, and Ru-RuO$_2$/MoO$_3$ CNRs-350, respectively. Moreover, the pore sizes for electrospun electrocatalysts are mainly concentrated around 3.0-3.4 nm.
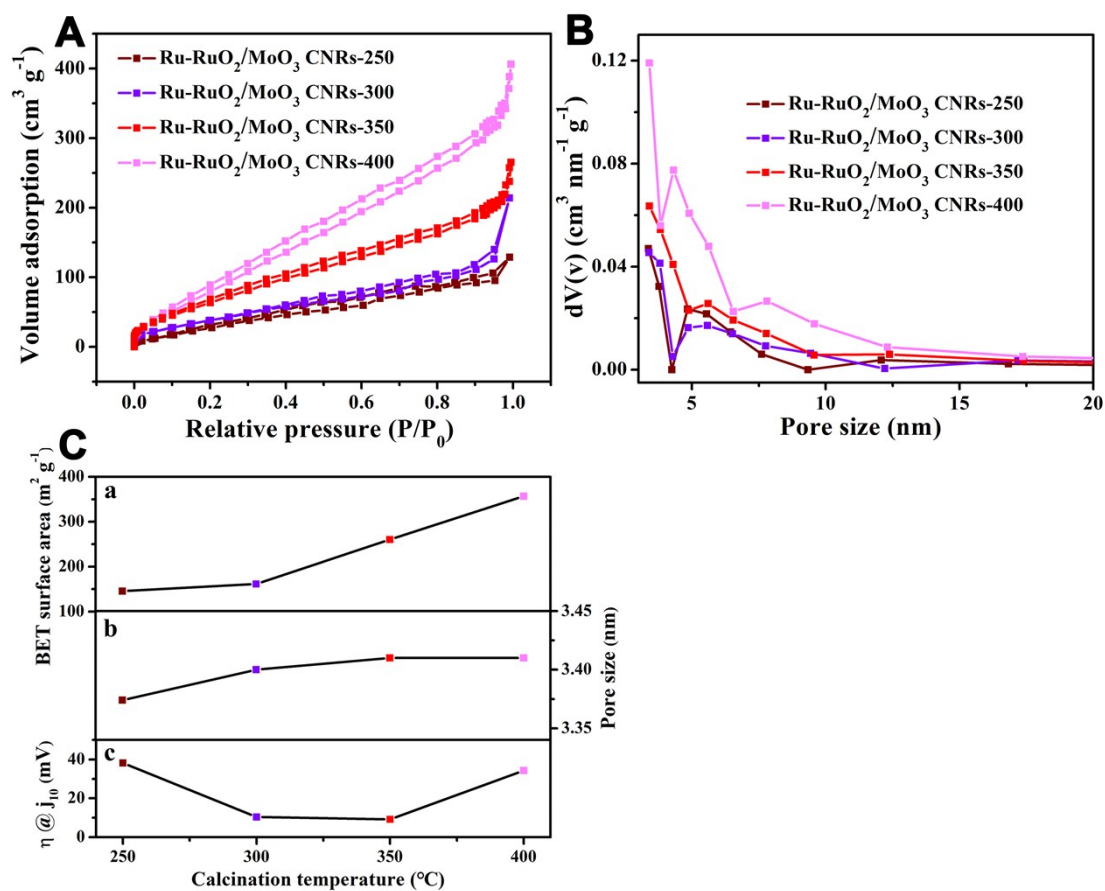
Fig. S8 (A) N_2 adsorption-desorption isotherms and (B) the corresponding BJH pore size distribution curves of Ru-RuO$_2$/MoO$_3$ CNRs-T, and (C) the relationship between calcination temperature and (a) BET surface area, (b) pore size, (c) HER activity.

It is clearly observed from Fig. S8 that the pore size and BET surface area of Ru-RuO$_2$/MoO$_3$ CNRs-T increase with the increasing of calcination temperature. However, as the calcination temperature rises, the HER activity (evaluated by overpotential at the current density of 10 mA cm^{-2}) of Ru-RuO$_2$/MoO$_3$ CNRs-T increases first and then decreases, indicating that the pore size and BET surface area are not the main factor affecting the HER activity of this series of electrocatalysts, as shown in the Fig. S8C. Hence, the ratio of Ru^{4+} to Ru^0 is the key to affecting the catalytic activity of these materials.
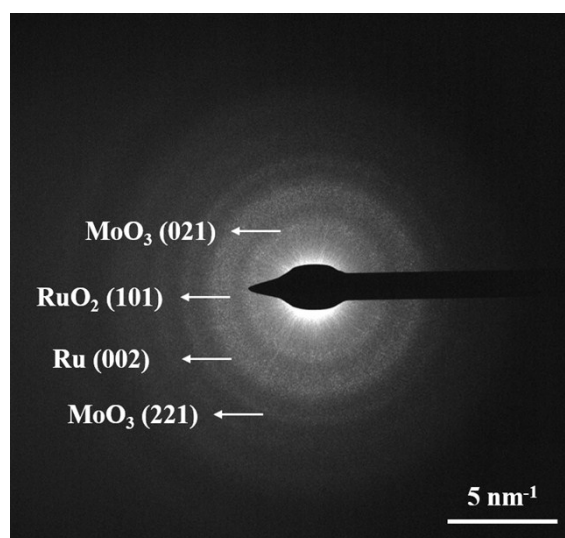
Fig. S9 SAED pattern of Ru-RuO$_2$/MoO$_3$ CNR-350.
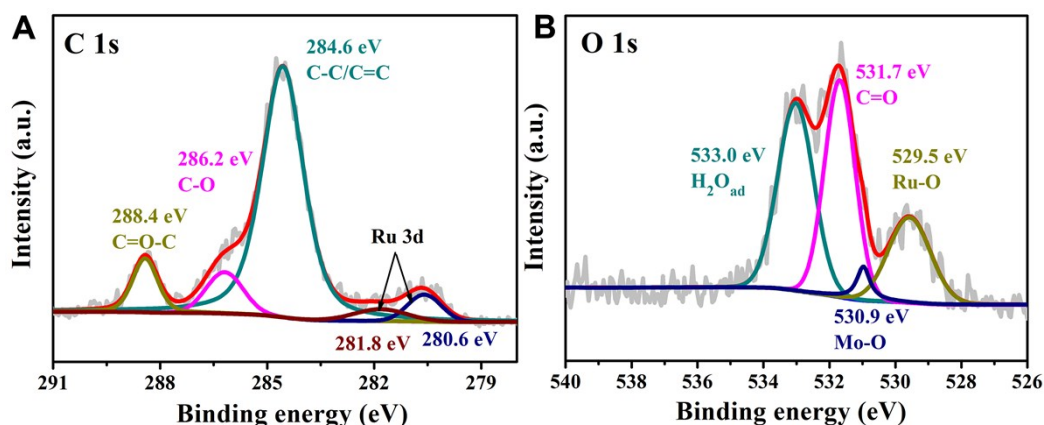
Fig. S10 High-resolution XPS spectra of (A) C 1s and (B) O 1s for Ru-RuO$_2$/MoO$_3$ CNRs-350.

The C 1s spectrum of Ru-RuO$_2$/MoO$_3$ CNRs-350 (Fig. S10A) can be divided into three main peaks are allocated to C-C/C=C (284.6 eV), C-O (286.2 eV) and C=O-C (288.4 eV)[4, 5]. There are two small peaks at around 280.6 and 281.8 eV are ascribed to the Ru 3d$_{5/2}$ of Ru^0 and Ru^{4+}, respectively[6, 7]. The high-resolution spectra of O 1s of Ru-RuO$_2$/MoO$_3$ CNRs-350 (Fig. S10B) appear two peaks at binding energy of 529.5 and 530.9 eV, which attributed to the Ru-O and Mo-O band, respectivily.[8-10] Furthermore, the peaks locating at 531.7 and 533.0 eV is corresponding to C=O band and surface-absorbed water.[11, 12]
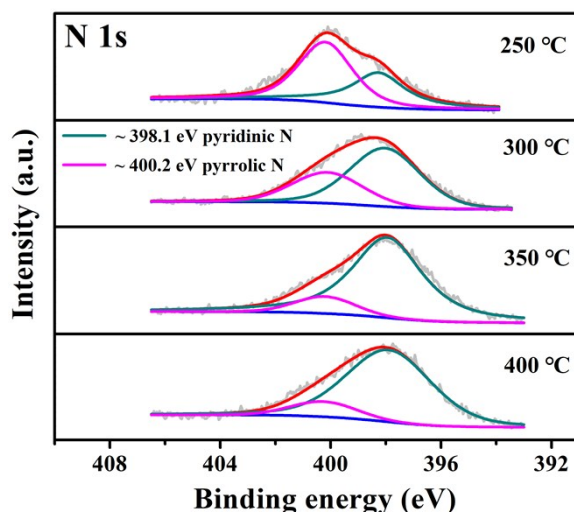
Fig. S11 High-resolution XPS spectra of N 1s and (B) O 1s for Ru-RuO$_2$/MoO$_3$ CNRs-T (T= 250, 300, 350, and 400 °C).

The N 1s spectra of Ru-RuO$_2$/MoO$_3$ CNRs-T were deconvoluted into two peaks, corresponding to two types of N species including pyridinic (398.1 eV) and pyrrolic (400.2 eV) [13, 14]. No peaks representing the coordination of N with Ru are detected by XPS, meaning that the N is more likely to bind to C than Ru under the experimental conditions   described   here.
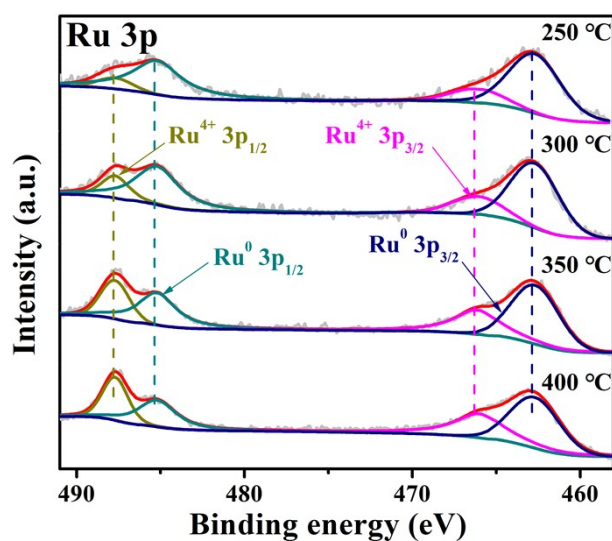
Fig. S12 High-resolution XPS spectra of Ru 3p for Ru-RuO$_2$/MoO$_3$ CNRs-T (T= 250, 300, 350, and 400 °C).

It can be seen from the Fig. S12 that the peaks of Ru^{4+} 3p gradually increase as the temperature rise, on the contrary, the peaks of Ru^0 3p decrease accordingly, which perfectly confirmed the XRD results. The ratios of Ru^{4+} to Ru^0 in Ru-RuO$_2$/MoO$_3$ CNRs-T are also calculated by integral area of corresponding peak, and the results are listed in the Table S1. The calculation result shows that the ratios of Ru^{4+} to Ru^0 increase from 1 : 4.3 to 1 : 1.4 as the temperature rise from 250 to 400 °C.

Table S1 Ratios of Ru^{4+} to Ru^0 in Ru-RuO$_2$/MoO$_3$ CNRs-T (T= 250, 300, 350, and 400 °C).

calcination temperature (°C)	Ru^{4+} : Ru^0
250	1 : 4.3
300	1 : 3.4
350	1 : 1.7
400	1 : 1.4
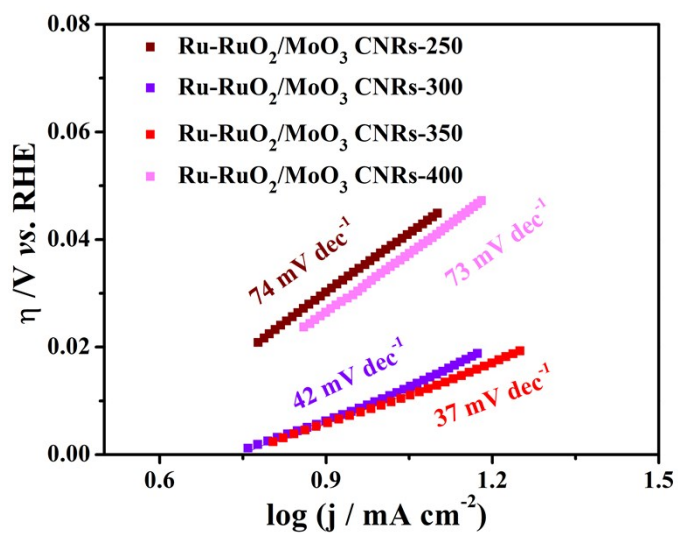
Fig. S13 Tafel plots for Ru-RuO$_2$/MoO$_3$ CNRs-T.
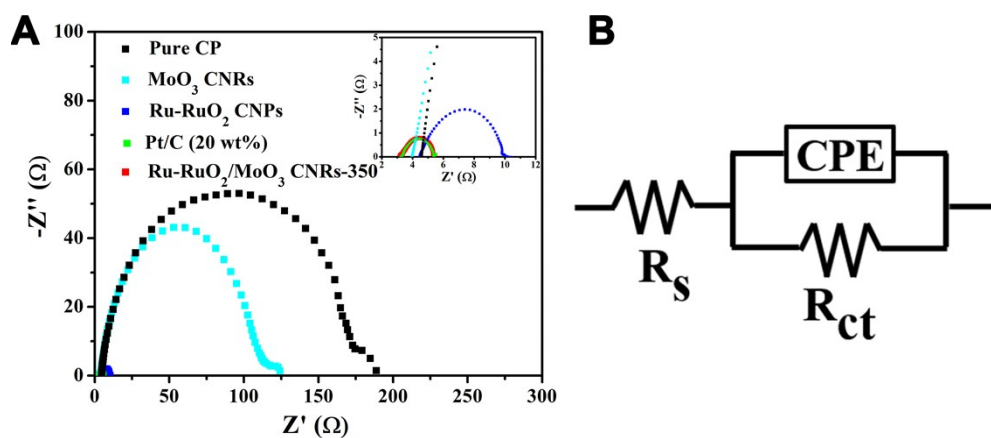
Fig. S14 (A) Nyquist plots for pure CP, MoO$_3$ CNRs, Ru-RuO$_2$ CNPs, Pt/C (20 wt %) and Ru-RuO$_2$/MoO$_3$ CNRs-350 (inset: the magnified image of high frequency region). (B) Equivalent circuit, in which R$_s$ and CPE are solution resistance and constant phase angle element, respectively.
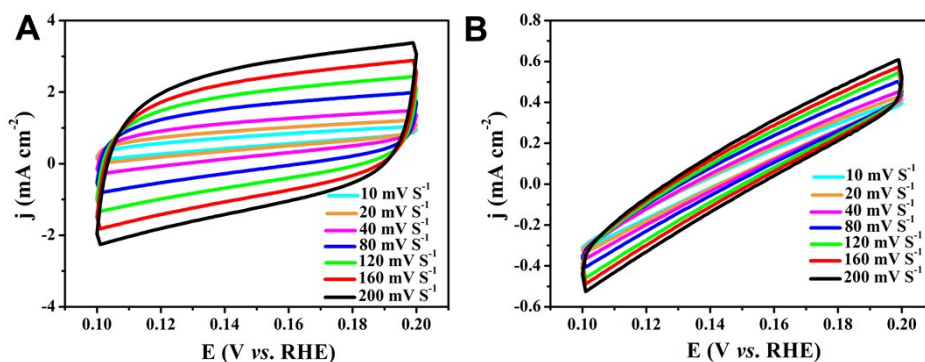
Fig. S15 CVs for (A) Ru-RuO$_2$ CNPs and (B) MoO$_3$ CNRs in 1.0 M KOH at different scan rates (10 - 200 mV S^{-1}).
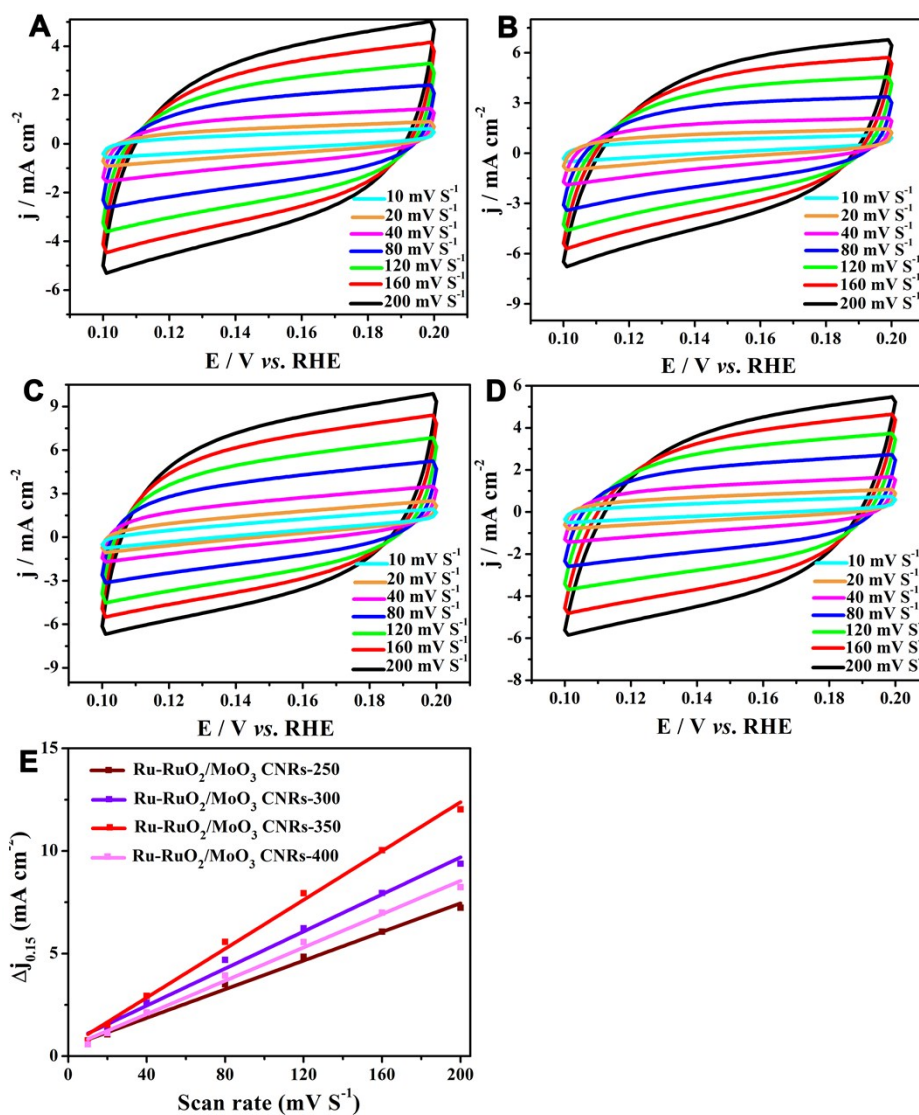
Fig. S16 CVs for (A) Ru-RuO$_2$/MoO$_3$ CNRs-250, (B) Ru-RuO$_2$/MoO$_3$ CNRs-300, (C) Ru-RuO$_2$/MoO$_3$ CNRs-350, and (D) Ru-RuO$_2$/MoO$_3$ CNRs-400 in 1.0 M KOH at different scan rates (10 - 200 mV S^{-1}). (E) The corresponding capacitive currents at 0.15 V vs. RHE as a function of scan rate for Ru-RuO$_2$/MoO$_3$ CNRs-T.
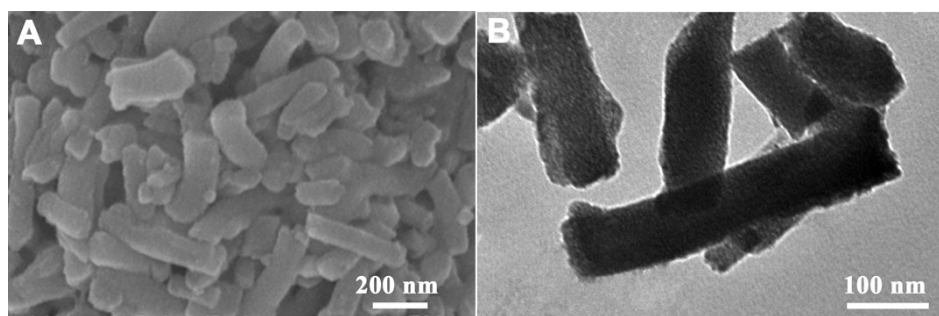
Fig. S17 (A) SEM and (B) TEM images of Ru-RuO$_2$/MoO$_3$ CNRs-350 after the stability test.
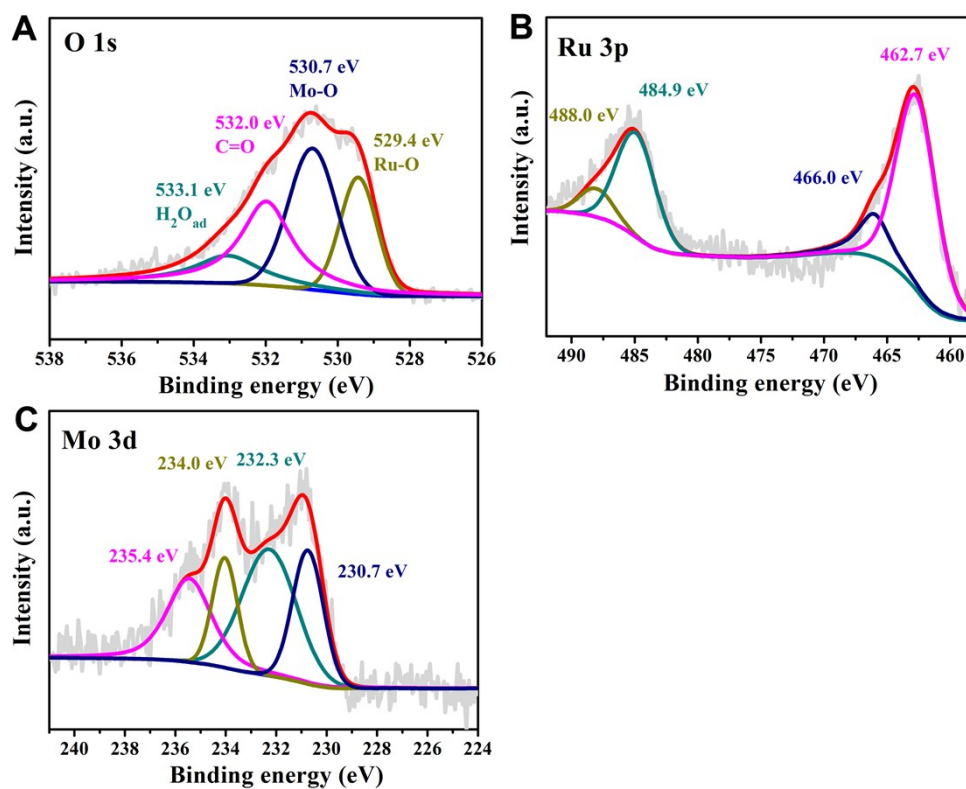
Fig. S18 High-resolution XPS spectra of (A) O 1s, (B) Ru 3p, and (C) Mo 3d for Ru-RuO$_2$/MoO$_3$ CNRs-350 after the stability test.

Table S2 Comparison of HER activity of the Ru-RuO$_2$/MoO$_3$ CNRs with other recently reported catalysts in alkaline medium.

Catalysts	Mass loading (mg cm^{-2})	Overpotential at 10 mA cm^{-2} (mV)	Tafel slope (mV dec^{-1})	References
Ru-RuO$_2$/MoO$_3$ CNRs	0.261	9.2	37	This work
Sr$_2$RuO$_4$	0.232	61	51	Ref. 15
RuO$_2$/N-C	0.306	40	44	Ref. 16
NiFeRu-LDH	not given	29	31	Ref. 17
RuIrO$_x$ (x $\geq$ 0)	0.01(Ru+Ir)	13	23	Ref. 18
RuO$_2$/NiO/NF	1.1	22	31.7	Ref. 8
Ru/Cu-doped RuO$_2$	0.285	28	35	Ref. 19
Ru/MoS$_2$/CP	1	13	60	Ref. 20
Ru-MoO$_2$ (S-2)	0.285	29	31	Ref. 21
Ir$_{0.80}$Ru$_{0.20}$O$_y$	not given	29.5	31.5	Ref. 22
rGO-MoO$_{3-x}$-MoRu	not given	20	25	Ref. 23
Ru-RuO$_2$/CNT	0.8	12	30	Ref. 2
Ru-MoS$_2$/CC	~ 12.44 (Ru: 46 µg cm^{-2})	41	114	Ref. 24

References

1. J. Wang, Y. Ji, R. Yin, Y. Li, Q. Shao and X. Huang, *J. Mater. Chem. A*, 2019, **7**, 6411-6416.

2. M. Zhang, J. Chen, H. Li, P. Cai, Y. Li and Z. Wen, *Nano energy*, 2019, **61**, 576-583.

3. M. Tariq, W. Q. Zaman, W. Sun, Z. Zhou, Y. Wu, L. Cao and J. Yang, *ACS Sustainable Chem. Eng.*, 2018, **6**, 4854-4862.

4. R. Wang, K. Lu, F. Zhang, Z. Tang and Y. Xu, *Appl. Catal. B Environ.*, 2018, **233**, 11-18.

5. M. Li, Z. Zhang, X. Ge, Z. Wei, Y. Yao, H. Chen, C. Wang, F. Du and G. Chen, *Chem. Eng. J.*, 2018, **331**, 203-210.

6. S. Sun, G. Wang, Y. Zhou, F. Wang and X. Xia, *ACS Appl. Mater. Interfaces*, 2019, **11**, 19176-19182.

7. S. Cao, J. R. Monnier, C. T. Williams, W. Diao and J. R. Regalbuto, *J. Catal.*, 2015, **326**, 69-81.

8. J. Liu, Y. Zheng, Y. Jiao, Z. Wang, Z. Lu, A. Vasileff and S. Qiao, *Small*, 2018, **14**, 1704073.

9. F. Haque, A. Zavabeti, B. Y. Zhang, R. S. Datta, Y. Yin, Z. Yi, Y. Wang, N. Mahmood, N. Pillai, N. Syed, H. Khan, A. Jannat, N. Wang, N. Medhekar, K. Kalantar-zadeh and J. Z. Ou, *J. Mater. Chem. A*, 2019, **7**, 257-268.

10. K. H. Kwak, D. W. Kim, Y. Kang and J. Suk, *J. Mater. Chem. A*, 2016, **4**, 16356-16367.

11. J. Mahmood, F. Li, C. Kim, H. Choi, O. Gwon, S. Jung, J. Seo, S. Cho, Y. Jub, H. Y. Jeongd, G. Kim and J. Baek, *Nano energy*, 2018, **44**, 304-310.

12. L. Sha, K. Ye, G. Wang, J. Shao, K. Zhu, K. Cheng, J. Yan, G. Wang and D. Cao, *J. Power Sources*, 2019, **412**, 265-271.

13. L. Yang, S. Feng, G. Xu, B. Wei and L. Zhang, *ACS Sustainable Chem. Eng.,* 2019, **7**, 5462-5475.

14. J. Yang, X. Wang, B. Li, L. Ma, L. Shi, Y. Xiong and H. Xu, *Adv. Funct. Mater.*, 2017, **27**, 1606497.

15. Y. Zhu, H. Tahini, Z. Hu, J. Dai, Y. Chen, H. Sun, W. Zhou, M. Liu, S. Smith, H. Wang and Z. Shao, *Nat. Commun.,* 2019, **10**, 149.

16. C. Yuan, Y. Jiang, Z. Zhao, S. Zhao, X. Zhou, T. Cheang and A. Xu, *ACS Sustainable Chem. Eng.* 2018, **6**, 11529-11535.

17. G. Chen, T. Wang, J. Zhang, P. Liu, H. Sun, X. Zhuang, M. Chen and X. Feng, *Adv. Mater.,* 2018, **30**, 1706279.

18. Z. Zhuang, Y. Wang, C. Xu, S. Liu, C. Chen, Q. Peng, Z. Zhuang, H. Xiao, Y. Pan, S. Lu, R. Yu, W. Cheong, X. Cao, K. Wu, K. Sun, Y. Wang, D. Wang, J. Li and Y. Li, *Nat. Commun.,* 2019, **10**, 4875.

19. K. Yang, P. Xu, Z. Lin, Y. Yang, P. Jiang, C. Wang, S. Liu, S. Gong, L. Hu and Q. Chen, *Small,* 2018, **14**, 201803009.

20. J. Liu, Y. Zheng, D. Zhu, A. Vasileff, T. Ling and S. Qiao, *Nanoscale,* 2017, **9**, 16616-16621.

21. P. Jiang, Y, Yang, R. Shi, G. Xia, J. Chen, J. Su and Q. Chen, *J. Mater. Chem. A,* 2017, **5**, 5475-5485.

22. Y. Cho, A. Yu, C. Lee, M. Kim and Y. Lee, *ACS Appl. Mater. Interfaces,* 2018, **10**, 541-549.

23. S. Liu, C. Chen, Y. Zhang, Q. Zheng, S. Zhang, X. Mu, C. Chen, J. Ma and S. Mu, *J. Mater. Chem. A,* 2019, **7**, 14466-14472.

24. D. Wang, Q. Li, C. Han, Z. Xing and X. Yang, *Appl. Catal. B Environ.,* 2019, **249**, 91-97.